

Ultra-broadband, high-contrast, high-resolution speckle imaging

Ryan Hall

Department of Physics and Astronomy, Georgia State University, Atlanta, GA, 30303, USA

Stuart M. Jefferies

*Department of Physics and Astronomy, Georgia State University, Atlanta, GA, 30303, USA
Institute for Astronomy, University of Hawaii, Pukalani, HI 96768, USA*

ABSTRACT

When observing targets in the near-Earth space environment using ground-based telescopes, the Earth's turbulent atmosphere and the telescope's aperture combine to act as a low-resolution spectrometer. The light at disparate wavelengths from a given point in the object lands at different spatial locations in the focal plane. Here we investigate the feasibility of capitalizing on this effect to provide snapshot hyper-spectral imaging of targets in the near-Earth space environment through ultra-broadband speckle imaging. In particular, we focus on the potential for using ultra-broadband speckle images for high-resolution, high-contrast imaging of closely spaced objects with a large contrast in brightness.

1. MOTIVATION

To comprehensively characterize a satellite for situational awareness, we need to know its type, location, orientation, purpose, and health (i.e., level of deterioration and functionality). Obtaining this information is a challenging problem, especially for satellites that are faint due to their size or distance away (or both). For example, we have limited surveillance capability for both the smallest objects in Low Earth Orbit (LEO) and satellites in the 4π -steradian volume of space from Geosynchronous Equatorial Orbit (GEO) out to cislunar orbit: a region of increasing concern. We also currently don't have a way to methodically monitor satellites' health, even the largest and closest ones.

Objects are characterized by their spatial, spectral, and temporal signatures. The holy grail for an object's characterization is a series of hyperspectral images that capture the full 3D surface area of the object in fine spatial and spectral detail. The latter data allow us to identify the object's materials, which sheds light on the object's capability. However, we are currently far from this ideal situation.

Although instruments for hyperspectral imaging exist, they typically require scanning in wavelength or one of the spatial dimensions. This limits the usefulness of these instruments to targets that are not rapidly changing pose. To the best of our knowledge, "snapshot" hyperspectral imaging of resolved targets (i.e., simultaneous acquisition of the spatial and spectral information), is still in its infancy, and there are no techniques in use for Space Domain Awareness (SDA). Here we investigate the potential for a novel snapshot hyperspectral imaging technique that leverages the diffractive properties of the imaging instrument's aperture and the dispersive properties of the atmosphere.

Diffraction and dispersion both cause light at different wavelengths from a point source, to land on spatially different locations in the image. That is, they produce a spectrally smeared signal. If we can unscramble the spectral information on the target that is inherently contained in a broadband image, then we have a way to perform snapshot hyperspectral imaging.

In addition to the benefits discussed above, we note that snapshot hyperspectral imaging over a wide wavelength range offers the improved capability for the detection of a faint object in proximity to a much brighter object. Accurate knowledge of the speckle structure in an image due to the brighter object requires knowledge of the spectrum of the target and how the light at different wavelengths is redistributed across the image. If we know this, we can remove the contribution to the signal from the bright object to facilitate the fainter object's detection. We note that in this context, bright means in relation to the faint object. The absolute brightness of the primary object can still be faint. As an

example, we may want to look for debris near a high-value asset in GEO. Here the brighter of the two objects is still dim.

In this paper, we focus on a proof-of-concept for the proposed atmosphere-instrument spectrometer concept. Is it even feasible to decode the spectral information on the target from a series of broadband speckle images? To answer this question, we investigate the relatively simple problem of two closely-spaced point-source objects of different brightness. With this type of object the signal's spectral spreading is not as smeared as it is for an extended object. The latter is a significantly more challenging problem to solve. In this preliminary feasibility study, we ignore photon noise and camera read noise.

2. SIMULATION SETUP

2.1 Phase Screen Generator

To simulate atmospheric turbulence's effects on a wavefront, we model the distributed turbulence along the propagation path using a number of discrete (infinitely thin) phase screens distributed along the path. The variation in the phase across each screen represents the fluctuations induced by changes of the refractive index in the atmosphere over the volume of space half-way to adjacent screens.

The simulator takes the initial wavefront and propagates it through a vacuum until it reaches a phase screen. It then repeats this process for the entire propagation path until every phase screen has perturbed the wavefront. This process is known as the split-step beam propagation method. We note that the propagation between the phase screens gives rise to amplitude fluctuations in the wavefront due to diffraction.

The level of turbulence in each phase screen is defined by the refractive index structure parameter (C_n^2). Since we are simulating vertical propagation, the C_n^2 will change at every phase screen. We calculate C_n^2 using the Hufnagel Valley approximation [7]:

$$C_n^2 = A \exp\left(-\frac{h}{H_A}\right) + B \exp\left(-\frac{h}{H_B}\right) + C h^{10} \exp\left(-\frac{h}{H_C}\right), \quad (1)$$

where h is the height above the ground (location along the propagation path). The A coefficient represents the strength of the ground layer of the atmosphere, and H_A is the height of its $1/e$ decay. B and H_B are similarly defined for the turbulence in the troposphere, and C and H_C are related to the turbulence peak located at the tropopause. We select the values of the coefficients such that the C_N^2 profile simulates the conditions at Mount Haleakala on Maui. We then slightly tweak the coefficients to obtain the desired Fried parameter. The resulting turbulence and physical parameters are listed in Table 1. At the end of the propagation process the wavefront is in the aperture plane of the optical system and the values are wrapped between π and $-\pi$. To unwrap the phase we use the Goldstein branch cut phase unwrapping algorithm [2]. We note that we have ignored the variation of the refractive index (n) on wavelength. This will need to be included in future studies.

Table 1: Table of simulation parameters

| | |
|---|---|
| Aperture diameter (D) | 3.6 m |
| Wavelength range | 400 - 1000 nm |
| Grid size | 1024 px |
| Side length | 7.2 m |
| Propagation distance | 31.25 km |
| Fried parameter (r_0 at $0.5 \mu\text{m}$) of wavefront in aperture | 11 cm |
| Hufnagel-Valley model coefficients | $A = 9.9 * 10^{-15}$, $H_A = 100$, $B = 9.9 * 10^{-16}$, $H_B = 1500$ $C = 8.1 * 10^{-53}$, $H_C = 1000$ |

2.2 Image generation

We assume that the field-of-view for our images is less than the size of the isoplanatic patch for the atmosphere during the observations. This then allows us to use the convolution model for image generation. We also assume that a broadband image can be modeled as a summation of monochromatic images and generate the observed broadband image using

$$I_{x,y} = \sum_{\lambda_1}^{\lambda_2} [(\Delta\lambda_1)O_\lambda \otimes PSF_\lambda]_{x,y}, \quad (2)$$

where O_λ is the true object at wavelength λ , PSF_λ is the point spread function (PSF) at the same wavelength, \otimes denotes convolution, $\lambda_2 - \lambda_1$ is the spectral bandwidth for the observation, and (x, y) are the image plane coordinates. The spectral bandwidth is sampled at N discrete wavelengths such that $\lambda_2 = \lambda_1 + N\Delta\lambda_1$. We use $\lambda_1=400$ nm and $\lambda_2=1000$ nm. This is the wavelength range over which silicon-based cameras have sensitivity. We set $\Delta\lambda=15$ nm and generate monochromatic images for $N = 40$ color planes. This sampling represents the change in wavelength needed to provide a subtle visible difference in the speckle morphology of the PSFs created using the wavefronts generated at two adjacent wavelengths near 400 nm.

For the object we use point sources to simulate two unresolved, closely spaced objects. For simplicity these sources are given by Blackbody spectra with different temperatures. We then generate a range of objects for our validation tests by varying the separation and difference in brightness of the objects.

The point spread function is modeled as

$$PSF_{x,y,\lambda} = |FT^{-1}(P(u, v) \exp -i\phi_\lambda(u, v))|^2 \quad (3)$$

where FT denotes Fourier transform, $P(u, v)$ and $\phi_\lambda(u, v)$ are the amplitude and phase of the simulated atmospheric wavefront, respectively, (u, v) are the Fourier plane coordinates, and $i = \sqrt{-1}$. For this work we use wavefronts that represent turbulence conditions of $D/r_0 = 33$. This simulates observations with the AEOS telescope on Mount Haleakala through median daytime seeing conditions during the Fall (see Table 1 of [1]).

Example images of the turbulence degraded object at selected monochromatic color planes, along with the ultra-broadband integrated over 40 color planes are shown in Fig. 1 for four different realizations of the atmosphere. The pixel scale of the images is set so that the data at 400nm are Nyquist sampled (i.e. 0.0138 arcsec/pixel).

2.3 Image reconstruction

For our initial investigation into the feasibility of recovering the original object from a set of broadband images, we assume we have a high-quality measurement of the PSF and that we only need to recover the object from a time series of observed broadband images. We then minimize the least-squares cost function

$$\varepsilon = \sum_k \sum_{x,y} (I_{k,x,y} - \hat{I}_{k,x,y})^2 = \sum_k \sum_{x,y} R_{k,x,y}^2, \quad (4)$$

where \hat{I} is the model of observed broadband image (I) given by

$$\hat{I}_{k,x,y} = \left[\sum_{\lambda_1}^{\lambda_2} (\Delta\lambda_2) \hat{O}_\lambda \otimes PSF_{k,\lambda} \right]_{x,y}, \quad (5)$$

\hat{O} is the modeled object, R is the residual difference between the observed and modeled images, and k is the frame index in the time series of images. Here $\lambda_2 - \lambda_1 = M\Delta\lambda_2$ where $M < N$. That is, we estimate the object at fewer color planes than were used to generate the broadband images. The pixels in the M color planes of \hat{O} are the variables in the minimization. We note the monochromatic PSF in Eqn. 5 represents an integral of N/M of the monochromatic PSFs used in the generation of the broadband images.

To minimize the cost function we use a gradient-based optimization algorithm called to the variable metric limited memory (vmlm). We calculate the gradient of the cost function with respect to the variables using

$$\frac{d\varepsilon}{dO_{x,y,\lambda}} = -2 \sum_k (R_k \star PSF_{k,\lambda})_{x,y} \quad (6)$$

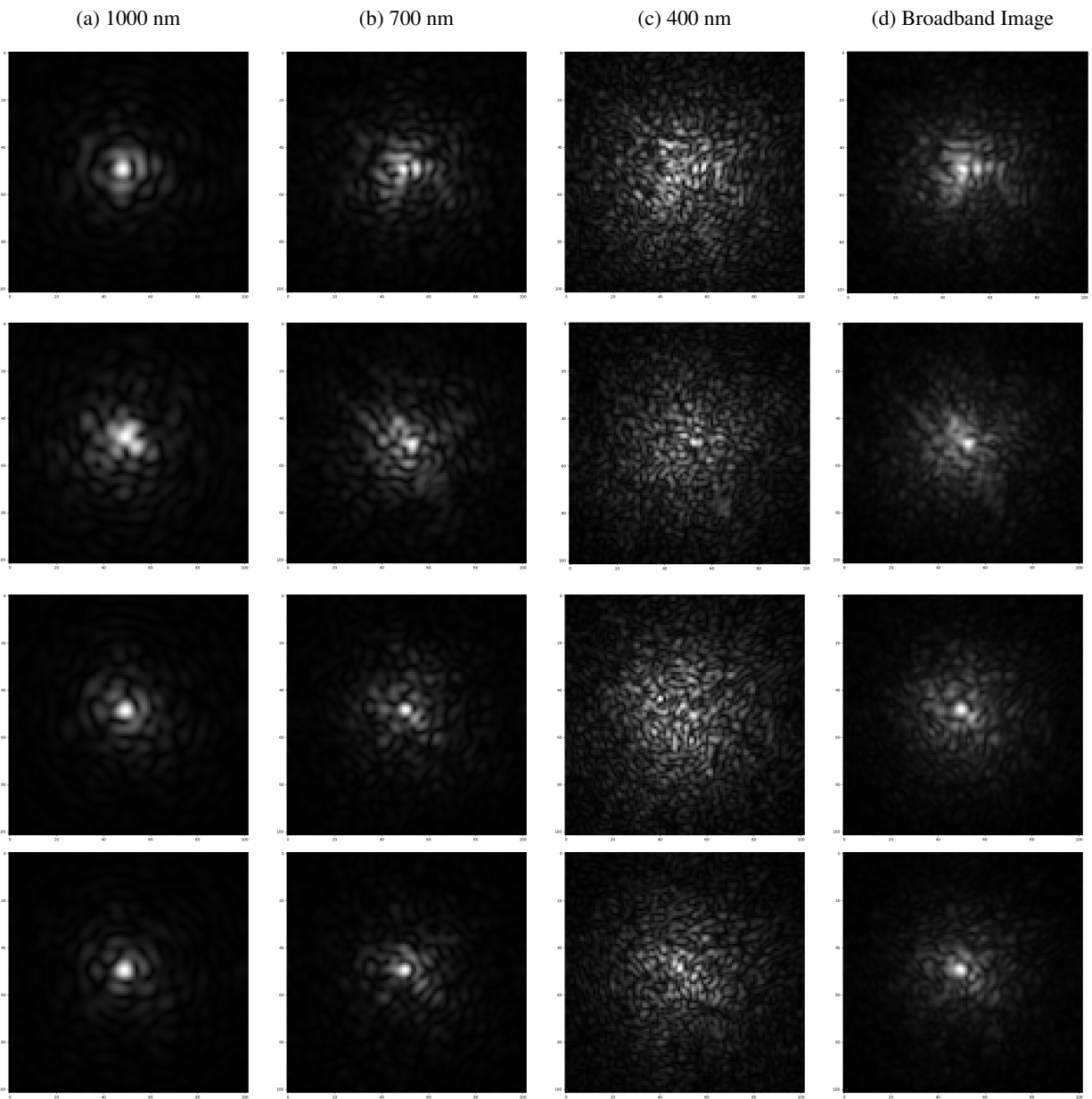


Fig. 1: A 4x4 array of simulated images of two closely spaced unresolved objects (contrast in brightness, secondary component:primary component, is 10^{-2}). The first three columns show, from left-to-right, the monochromatic image for the color planes at 1000 nm, 700 nm, and 400 nm. These images show how the morphology of the speckle structure changes with wavelength due to diffraction. The final column on the right is the full integrated broadband image over all 40 color planes. All images are shown using a square root intensity display to highlight the extent of the speckle structure. The four rows show four realization of the atmosphere.

This is computationally more efficient than using numerical derivatives.

For our validation tests we generate broadband data sets for two separations between the two unresolved objects (0.69 arc-seconds and 0.14 arc-seconds), and two contrast ratios for each separation (the brightness of the secondary component is 10^{-2} and 10^{-3} of the brightness of the primary component).

For all the reconstructions presented in the paper we use $k = 11$ broadband images and allow 1,000 iterations in the minimization routine.

3. RESULTS

For our initial proof-of-concept tests we assume we have perfect knowledge of the wavefront phase for each of the M color planes of every broadband image. Our first two data sets represent the two unresolved objects at 0.69 arc-second separation with a contrast ratio of 10^{-2} and 10^{-3} . The spectral recoveries for the two components of the object are shown in Fig. 2. In both cases the spectrum of the bright component is well recovered. This validates our hypothesis that spectral information on a target can be recovered from a series of ultra-broadband speckle images. Interestingly, the recovered spectrum for the secondary component is a reasonable representation of the truth spectrum when the contrast is 10^{-2} . This suggests the spectral recovery is robust over a useful dynamic range. When the brightness of the secondary decreases to 10^{-3} of the primary object, the recovered spectrum for the former has little similarity to the truth spectrum. If we are just interested in the detection of the faint companion, however, then we can integrate the recovered object over all color planes. In this case we find for both contrast scenarios that 99% of the counts for the primary component are recovered, while the recovery of the secondary components varies slightly between the two contrast ratios: at 10^{-2} contrast 90% of counts are recovered while at 10^{-3} , 88% are recovered. That is, the secondary component is clearly seen in the restored images, even at the lowest contrast of 10^{-3} .

To assess the applicability of ultra broadband speckle imaging for high-resolution, high-contrast imaging, we ran some additional tests where we reduced the separation between the two unresolved objects to 0.14 arc-seconds. The results

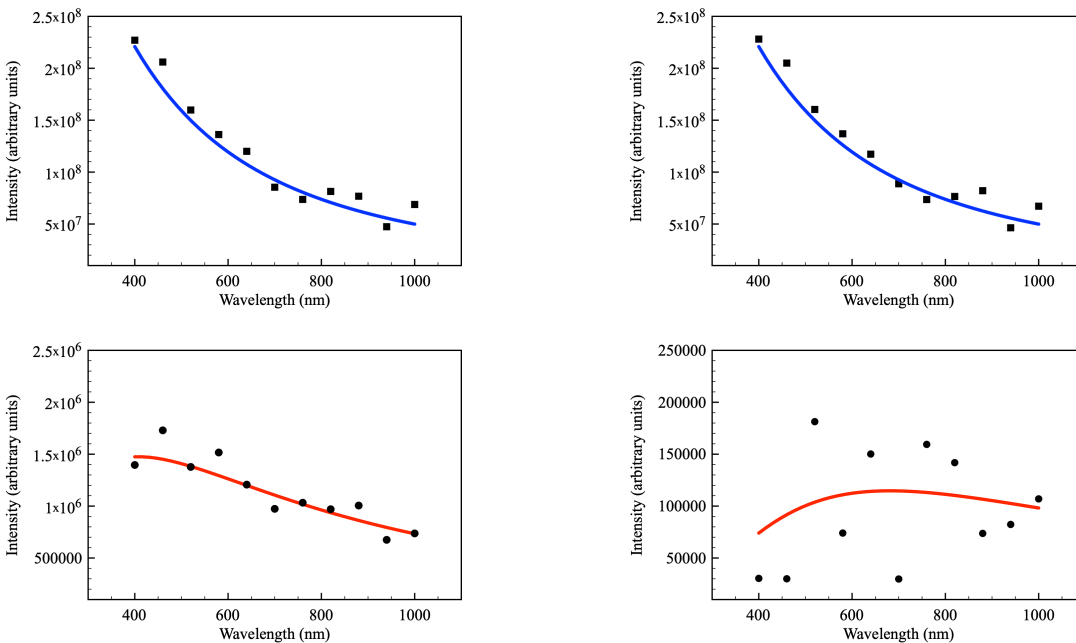


Fig. 2: Recovered and truth spectrum for primary and secondary objects separated by 0.69 arc-seconds. The top row shows the results for the bright (primary) object, and the bottom row shows the results for the dim (secondary) object. The left-hand column represents a secondary:primary contrast in brightness of 10^{-2} and the right column represents a contrast of 10^{-3} . The solid line shows the true spectrum and the solid symbols denote the recovered values in the 11 color planes used to model the object.

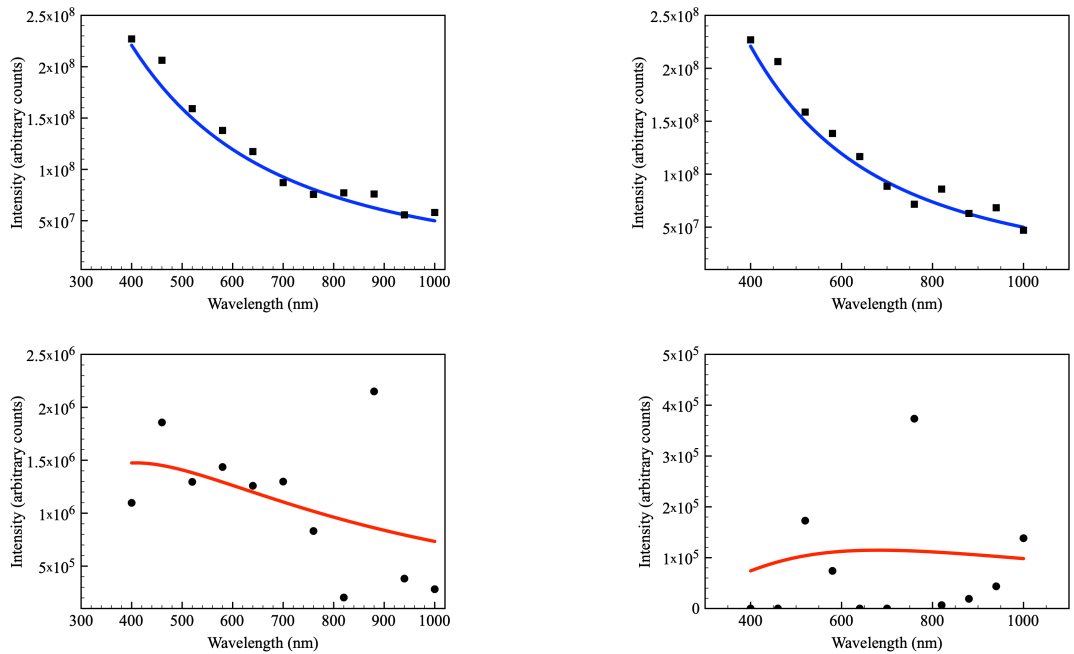


Fig. 3: Recovered and truth spectrum for primary and secondary objects separated by 0.14 arc-seconds. The top row shows the results for the bright (primary) object, and the bottom row shows the results for the dim (secondary) object. The left-hand column represents a secondary:primary contrast in brightness of 10^{-2} and the right column represents a contrast of 10^{-3} . The solid line shows the true spectrum and the solid symbols denote the recovered values in the 11 color planes used to model the object.

are shown in Fig. 3. This figure shows that the primary component is recovered with similar accuracy to the earlier results for the 0.69 arc-second separation. As seen in Fig. 3, the secondary component loses some accuracy compared to its counterpart in Fig. 2, however, 95% of the total counts are still recovered. Finally, at 10^{-3} contrast, although the secondary component's recovered spectrum is a poor representation of the truth spectrum, the integrated flux of the secondary component still shows 67% of the true flux. Looking at the spectrally integrated recovered object in Fig. 4, it can be seen that the background is very clean and the secondary component is clearly visible. This suggests the potential for high-contrast, high-resolution imaging. We note that all of the above results were obtained using

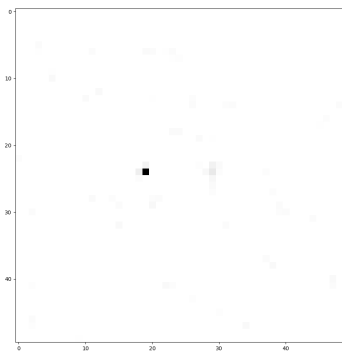


Fig. 4: The recovered image of two point sources separated by 0.14 arc-seconds with 10^{-3} contrast, integrated over the 11 color planes used to model the object. The image is shown in the negative gray scale with a third root display of intensity to emphasize the dimmer secondary component in proximity to the brighter primary component.

11 frames. In practice, hundreds (or thousands) of frames will be available. Increasing the number of frames in the restoration will improve the recoveries' fidelity and allow us to reach high contrast values. As an example, Hope et al.

[3] showed that using 2,000 frames of monochromatic speckle data obtained on an 8-meter telescope, they can detect a secondary object whose brightness is 10^{-4} of the brightness of the primary object.

For our last test, we relax the requirement on the fidelity of the PSF. Again, we use the binary target, this time with a separation of 0.69 arc-seconds and a contrast of 6.2×10^{-3} between the two components. We replace the truth PSFs at each wavelength with PSFs generated from wavefronts with a root-mean-square error of 0.69 radians with respect to the truth wavefronts. This was done by smoothing the truth phases with a Gaussian kernel, which removes the wavefront's high spatial frequencies. This level of wavefront error at $D/r_0 = 33$ is commensurate with the performance that can be obtained with an imaging Shack-Hartmann wavefront sensor and multi-aperture phase retrieval of the WFS data [4]. We note the impact of the missing high-spatial frequency information on the morphology of PSFs will increase as the wavelength decreases. The results in Fig. 5 are similar to the results obtained with perfect knowledge of the PSFs, and suggest that the restoration's quality is not highly sensitive to the fidelity of the PSF estimates. This characteristic offers hope for the practical realization of ultra-broadband speckle imaging.

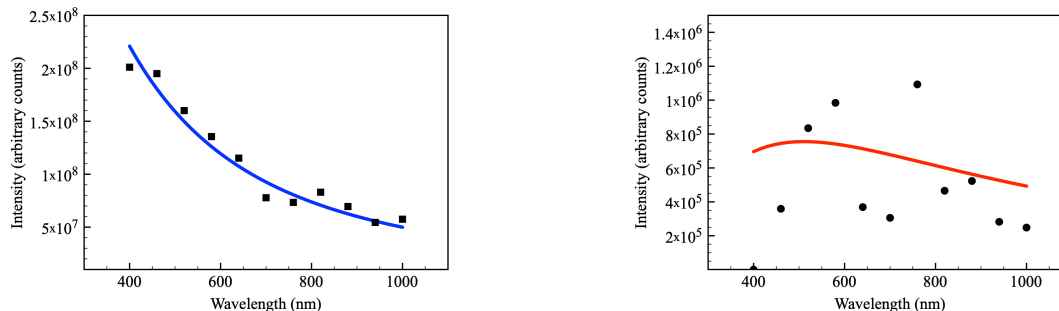


Fig. 5: Recovered and truth spectrum for primary and secondary objects separated by 0.1 arc-seconds and a contrast ratio of 6.2×10^{-3} , using degraded PSFs (see main text for details). The left panel shows the results for the bright (primary) object, and the right panel shows the results for the dim (secondary) object. The solid line shows the true spectrum and the solid symbols denote the recovered values in the 11 color planes used to model the object.

4. DISCUSSION

We have shown that for the highly idealized case of an unresolved binary object observed through $D/r_0 = 33$ turbulence, without photon and read noise, it is feasible to recover the spectral information on the target from a series of ultra-broadband images when we have high-quality estimates of the atmospheric PSFs and their variation with wavelength. Fortunately, recent advances in wavefront sensing offer the possibility of high-fidelity PSF measurements [6]. We note that the results presented here are based on a limited number of ultra-broadband images. In practice, thousands of images will be available. Also, the minimization was limited to 1,000 iterations. Extending both the number of frames in the restoration, and the number of iterations for the minimization will lead to improved restorations. Lastly, we can improve any measured estimates of the wavefronts using the blind deconvolution technique (e.g., [4]) during the image restoration process. In this case, we note that broadband images are inherently a source of wavelength diverse information. As such, they should provide leverage in the blind deconvolution restoration [5].

In conclusion, our results show that extracting spectral information on the target object from a set of turbulence degraded broadband images is feasible. We have also demonstrated that this capability may help detect closely spaced objects when one object is significantly brighter than the other.

We note that although these initial studies are encouraging, they represent just the tip of the iceberg. There is a lot more research required on ultra-broadband speckle imaging before we can claim it is a viable approach for snapshot hyper-spectral imaging for space domain awareness.

5. ACKNOWLEDGEMENTS

The Air Force Office of Scientific Research funded this work through contract FA9550-14-1-0178. RH thanks Dr. Rao Gudimetla and Dr. Mark Spencer for their mentoring on atmospheric turbulence during the summers of 2018 and

2019 under the Air Force Research Laboratory's Scholars Program. SMJ thanks Douglas Hope and Michael Hart for discussions about ultra-broadband imaging.

6. REFERENCES

- [1] W. Bradford. Maui4: a 24 hour Haleakala turbulence profile. Proceedings of the Advanced Maui Optical and Space Surveillance Technologies Conference held in Wailea Maui Hawaii September 14–17, 2010. Ed.: S. Ryan Maui Economic Development Board, 2010.
- [2] R. M. Goldstein, H. A. Zebker, L. Werner. Satellite Radar Interferometry: Two-Dimensional Phase Unwrapping. *Radio Sci*, 23(4), 713- 720, 1988
- [3] D. A. Hope, S. M. Jefferies, M. Stangalini, F. Pedichini, G. Li Causi, M. Mattioli, and S. Antonucci. High-resolution, high-contrast, imaging of small objects near satellites. Proceedings of the Advanced Maui Optical and Space Surveillance Technologies Conference held in Wailea Maui Hawaii September 17-20, 2019. Ed.: S. Ryan Maui Economic Development Board, 2019.
- [4] D. Hope, S. M. Jefferies, M. Hart, and J. Nagy. High-resolution speckle imaging through strong atmospheric turbulence. *Optics Express*, 24, 12116-12129, 2016.
- [5] H. R. Ingleby and D. R. McGaughey. Real data results with wavelength-diverse blind deconvolution. *Optics Letters*, 30, 489-491, 2005.
- [6] S. M. Jefferies, D. A. Hope, A. Thrasher, and M. Willson. Tomographic wave-front sensing using multi-aperture phase retrieval and the frozen flow hypothesis. *Optics Letters*, in preparation, 2020.
- [7] J. L. Mohr, R. A. Johnston, P. L. Cottrell. Optical Turbulence Measurements and Models for Mount John University Observatory. *Publications of the Astronomical Society of Australia*, Volume 27, Issue 3, pp. 347-359, 2010.